



Electrochemical and *In Situ* XRD Studies of the Li Reaction with Combinatorially Sputtered $\text{Mo}_{1-x}\text{Sn}_x$ ($0 \leq x \leq 0.50$) Thin Films

A. Bonakdarpour,^a K. C. Hewitt,^a R. L. Turner,^{b,*} and J. R. Dahn^{a,*z}

^aDepartment of Physics, Dalhousie University, Halifax, Nova Scotia, B3H 3J5, Canada

^b3M Company, 3M Center, St. Paul, Minnesota, 55144, USA

Detailed electrochemical studies of the reaction of Li with combinatorially sputter-deposited BCC ($x \leq 0.4$) and nanocrystalline ($x \geq 0.4$) $\text{Mo}_{1-x}\text{Sn}_x$ thin films are reported for $0.05 \leq x \leq 0.5$. *In situ* X-ray diffraction (XRD) performed for $x = 0.22, 0.36, 0.44$, show no evidence for formation of new phases during the reaction with Li. During charge/discharge cycling, a definite and periodic variation of the BCC $\text{Mo}_{1-x}\text{Sn}_x$ (110) Bragg angle for $x \leq 0.40$ is strong evidence for a topotactic Li insertion mechanism. Sensitive differential capacity (dq/dV vs. V) measurements on $\text{Li}/\text{Mo}_{1-x}\text{Sn}_x$ cells with $x \leq 0.36$ show no new peaks for as many 75 cycles, supporting a topotactic insertion reaction. However, in the higher Sn content films ($x \geq 0.4$), the appearance and growth of new dq/dV peaks after the first cycle is consistent with the aggregation of Sn clusters and the formation of Li-Sn phases. Inclusion of about 20% oxygen in nanostructured films seems to prevent Sn aggregation and improve the cycling performance markedly. The best materials give specific capacities near 350 mAh/g, have densities near 9 g/cc and cycle well. This could be the first report of true topotactic Li insertion into a metal host.

© 2004 The Electrochemical Society. [DOI: 10.1149/1.1646138] All rights reserved.

Manuscript submitted November 14, 2002; revised manuscript received August 20, 2003. Available electronically February 11, 2004.

The need for higher energy Li-ion battery electrode materials with higher energy has driven research on both cathode and anode materials. For anode materials, research has centered on active elements like Sn or Si, which alloy with Li and have gravimetric and volumetric capacities up to ten times that of graphite commonly used in today's commercial Li-ion batteries. However, crystalline binary Li alloys Li_xM ($\text{M} = \text{Si}, \text{Sn}, \text{Al}$), suffer from severe grain fragmentation during lithiation/delithiation because coexisting phases with different Li concentrations lead to inhomogeneous volume expansions. Cracking of the alloy grains results in loss of electrical contact or poor conductivity and this hinders the long term cycling performance.¹

For instance, Li_xSn goes through five different crystallographic phases for ($0 < x < 4.2$) and the volume changes are as large as 300%. As a remedy, Besenhard *et al.* suggested the incorporation of nanosized active alloying species like Sn in an inactive matrix of SnSb, in order to suppress Li-Sn phase transitions and improve the cycling behavior.² Nanosized active Sn_2Fe mixed with inactive SnFe_3C has also shown improved performance.³

One very appealing idea would be to synthesize a high capacity, low-voltage, Sn-based (or other active element) insertion material, which is truly topotactic *i.e.*, the host retains its structure during Li insertion/removal and hundreds of cycles can be obtained without any significant loss of capacity. The Li insertion reaction in layered structures like Li_xCoO_2 and Li_xC_6 is topotactic. The reaction of Li in ternary systems like LiMM' , where M is an alloying element and M' is an inactive element like Cu_6Sn_5 and InSb, have been suggested to be insertion/displacement reactions that subsequently show reactions with small volume expansions upon reaction with Li.^{4,5} In fact, both Cu_6Sn_5 and InSb were first reported to show some regions of topotactic Li insertion; however further research showed that the reaction of Li with these intermetallic compounds is more subtle.

For Cu_6Sn_5 , careful *in situ* X-ray and Mossbauer experiments by Larcher *et al.*⁶ and Fransson *et al.*⁷ showed that upon full lithiation Cu is extruded from $\text{Li}_2\text{Cu}_6\text{Sn}_5$ yielding $\text{Li}_{4.4}\text{Sn}$ and Cu as final products. The charge reaction is not completely reversible and cycling performance improves somewhat only when $\text{Li}/\text{Cu}_6\text{Sn}_5$ cells are discharged only to 0.2 V (or to a limiting composition of $\text{Li}_2\text{Cu}_6\text{Sn}_5$), preventing Cu extrusion. For InSb, the full reaction

with Li causes the destruction of the compound and the formation of Li_3Sb , LiIn , and Li_3In_2 phases.⁸ Neither Cu_6Sn_5 or InSb is a topotactic Li insertion compound over the entire voltage range. The $\text{Mo}_{1-x}\text{Sn}_x$ phases reported here, however, may indeed insert Li reversibly during charge/discharge for $x < 0.36$, even when discharged to 0 V.

In an earlier paper⁹ we reported the properties of sequentially sputtered Mo-Sn films, where a variety of crystal structures and nanostructures were obtained depending on the composition and the sputtering conditions. We prepared crystalline BCC $\text{Mo}_{1-x}\text{Sn}_x$ ($x < 0.42$), nanocrystalline BCC $\text{Mo}_{1-x}\text{Sn}_x$ coexisting with nanocrystalline Sn ($x > 0.45$), and nanoscopic regions of Sn embedded in lamina of composition modulated $\text{Mo}_{1-x}\text{Sn}_x$ ($x > 0.4$).⁹ The electrochemical behavior of the films for $x < 0.5$ were very promising, for example nanostructured $\text{Mo}_{0.5}\text{Sn}_{0.5}$ delivered about 250 mAh/g for about 200 cycles.¹⁰ We therefore decided to prepare and study the composition range $0 < x < 0.5$ in $\text{Mo}_{1-x}\text{Sn}_x$ using the methods of combinatorial materials science (CMS).

Combinatorial chemistry, or parallel fabrication and rapid screening of new materials, has been a well-established method in the discovery of new pharmaceutical drugs.¹¹ In the past decade, however, based on the pioneering work of J. J. Hanak¹² and coworkers in the 1970s, Berkeley researchers including X. D. Xiang and P. G. Schultz¹³ developed and applied sophisticated combinatorial techniques to synthesize and study solid materials like HT_c superconductors, dielectrics, and fuel cell catalysts. Combinatorial electrochemistry was perhaps first introduced by Reddington *et al.* who described a method of producing libraries of metal alloy catalysts for methanol oxidation, whereby a few hundred combinations of metals were printed on Toray paper and screened for their catalytic activity.¹⁴ In the search for anode and cathode materials for Li-ion batteries, we recently developed a simple but powerful sputtering-based methodology, which can continuously map the composition spaces of materials in 1 and 2 dimensional thin film libraries. Two to four targets, which can be elements or compounds, are sputtered simultaneously and the sputtered beams are masked to obtain the desired composition variation in the films. A detailed description of our approach is reported elsewhere.¹⁵

The broad objective of this study has been really twofold: First to establish a CMS technique to synthesize and characterize composition-graded films and second to use these films in the search for new anode materials for Li-ion batteries. The deposition, composition and structure of the $\text{Mo}_{1-x}\text{Sn}_x$ films studied here are reported in a related paper.¹⁶ Here, we will present the electrochemical

* Electrochemical Society Active Member.

^z E-mail: jeff.dahn@dal.ca

Table I. Summary of Mo-Sn sputtering experiments used for electrochemical studies.

Growth ID	Ar Flow rate (sccm)	Argon pressure (mTorr)	Sn (P/V/I) ^b (W/V/A)	Mo (P/V/I) (W/V/A)	Sputtering time (hours)	Rotation speed (rpm)
Run129 ^a	15	2	125/376/0.33	300/332/0.90	10	25
SPD74	2.5	3.2	50/346/0.15	149/362/0.41	6	30
SPD99	8.5	10	25/274/0.09	75/255/0.30	5.8	23
SPD103	1.0	1.8	25/378/0.23	75/323/0.23	6.0	23
SPE5	0.6	1.5	28/339/0.08	75/315/0.231	9.0	17
SPE21	0.6	1.4	28/313/0.085	75/295/0.247	9.0	17
SPF6 ^c	0.90	1.0	25/358/0.06	117/494/0.233	1.5	17
SPF66	1.0	1.0	35/339/0.1	100/337/0.29	2.5	17
SPG30	3.5Ar/0.5O ₂	3.5	49/283/0.163	150/290/0.515	2.5	30

^a Run129 was deposited at a larger target-substrate distance thus a longer time.

^b P = power, V = voltage, and I = current.

^c For SPF6 no masks were used, the growth was aimed at a fixed composition of $x = 0.30$.

properties of these films and provide evidence for a topotactic Li insertion mechanism in Mo_{1-x}Sn_x ($x < 0.36$). We also discuss the role of long range ordering (*i.e.*, crystalline *vs.* nanocrystalline) and oxygen in the host on the voltage profile, specific capacity, and cycling performance. In this paper, we refer to the discharge of Li/Mo_{1-x}Sn_x cells as the direction of current flow that occurs when the cells are connected to a resistive load, as is common practice. This means that discharge of the cells corresponds to adding Li to Mo_{1-x}Sn_x and charge of the cells corresponds to removing Li from Mo_{1-x}Sn_x.

Experimental

A detailed description of our combinatorial approach and thin film deposition procedures for Mo_{1-x}Sn_x are reported in a complementary paper, but will be briefly recapitulated here.¹⁵ The composition range $0 < x < x_{\max}$ in Mo_{1-x}Sn_x was produced in a single sputter deposition by a Corona Vacuum Coaters V3T magnetron sputtering system which reaches a base pressure of about 7×10^{-8} Torr. Two-inch diameter targets of 99.9% pure Mo and Sn

(Kurt J. Lesker) were sputtered by dc power supplies (Advanced Energy MDX-1K) onto 1.3 cm diam Cu disks for electrochemical cells, onto 3.0×1.0 in. glass microscope slides for X-ray diffraction (XRD) and microprobe analysis, and onto Be disks for *in situ* XRD studies. All substrates were coated in the same sputtering run.

To map out the stoichiometry of the film, a mask was designed and placed in front of the Mo target. This mask causes constant Mo deposition (mass per unit area) *vs.* position on the substrate table that rotates during the deposition. A different shaped mask in front of Sn target causes a linearly varying Sn deposition *vs.* radius on the substrate. By first measuring the deposition rates of Mo and Sn and then adjusting the sputtering powers one can control the value of x_{\max} in Mo_{1-x}Sn_x ($0 < x < x_{\max}$).¹⁵ The table was rotated at about 30 rpm during the sputtering runs and this lead to an intimate mixture of the sputtered Mo and Sn atoms. The sputtered region is a donut-shaped ring with an inner radius of 9.5 cm and an outer radius of 17 cm. At the inner radius, the composition is $x = x_{\max}$ in Mo_{1-x}Sn_x and at the outer radius the composition is $x = 0$ in Mo_{1-x}Sn_x. The sputtering parameters, including pressure, power,

Table II. Summary of the structure and composition of the Mo-Sn sputtered films.

ID	x in Mo _{1-x} Sn _x	y in [MoSn] _{1-y} O _y	Thickness t (μm)	Structure and phases
SPD74	0.04-0.47	0.44 to 0.22	$0.65 < t < 1.2$	Nanosized BCC for $x > 0.12$ Single phase rock salt for $x < 0.12$, possibly a Mo-O phase
SPD99	0.02-0.36	~ 0.4	$0.04 < t < 0.85$	Broad BCC peaks "powder-like" pattern
SPD103	0.05-0.92	~ 0.1		Crystalline Sn for $x \sim 0.91$ Nanosized BCC (Mo _{0.63} Sn _{0.37}) and Sn for $0.37 < x < 0.9$ Nanosized and crystalline BCC for $x \approx 0.34$ BCC and Mo ₃ Sn-type for $0.1 < x < 0.33$ BCC phase below $x = 0.1$
SPE5	0.02-0.50	None for $0.3 < x < 0.5$ ~ 0.10 for $x < 0.3$	$0.7 < t < 1.64$	Nanosized BCC for $x \approx 0.36$, Crystalline BCC for $x < 0.36$
SPE21	0.03-0.5	None for $x > 0.25$ ~ 0.06 for $x > 0.25$	$0.75 < t < 1.9$	BCC and Mo ₃ Sn mixture for $0.11 < x < 0.31$ Nanosized BCC for $x > 0.40$, Crystalline BCC for $x < 0.40$
SPF6	0.30	~ 0.05	~ 1	BCC and Mo ₃ Sn for $0.10 < x < 0.33$ BCC for $x < 0.10$
SPF66	0.05-0.5	0 for $x < 0.2$ 0.05 for $x > 0.2$		BCC phase BCC for $0.05 < x < 0.38$
SPG30	0.02-0.44	0.2 < y < 0.5 for $0.02 < x < 0.5$	$0.5 < t < 1.3$	Nanocrystalline for $x > 0.38$ Nanocrystalline

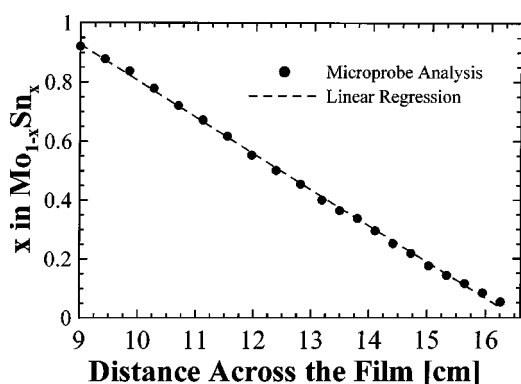


Figure 1. x in $\text{Mo}_{1-x}\text{Sn}_x$, as measured by electron microprobe, vs. position for a film (SPD103) sputter deposited on a glass microscope slide using combinatorial methods.

voltage, and current for the different sample films are summarized in Table I.

Composition analysis of the films was made using a JEOL JXA-8200 Superprobe equipped with one energy dispersive (EDS) spectrometer, five wavelength dispersive (WDS) spectrometers, and an automated motion stage. The metal content (Mo, Sn, and Cu/Si substrate), was measured by EDS and the oxygen content was analyzed by WDS.

For rapid structural analysis of the entire composition range deposited on a glass slide, an Inel curved position sensitive detector (CPS 120) and a PW-1720 Phillips X-ray generator using $\text{Cu K}\alpha$ radiation was used. The system is equipped with an automated x-y motion stage, which makes it an ideal tool for analyzing combina-

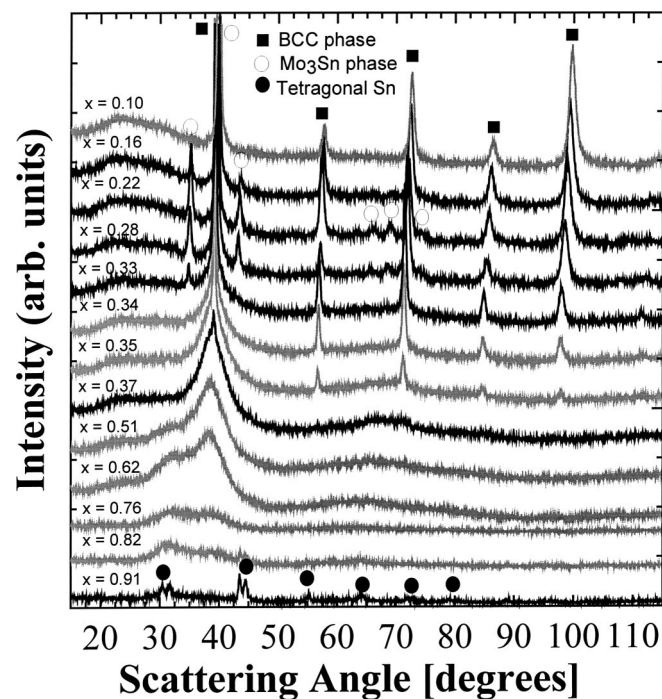


Figure 2. XRD patterns taken at different positions on the slide described by Fig. 1. The structure changes from crystalline tetragonal Sn (near $x = 0.91$) to BCC $\text{Mo}_{0.9}\text{Sn}_{0.1}$. Open circles, solid squares, and solid circles denote Mo_3Sn -type, BCC $\text{Mo}_{1-x}\text{Sn}_x$, and crystalline Sn, respectively. Near $2\theta = 40^\circ$, peaks of the BCC $\text{Mo}_{1-x}\text{Sn}_x$ phase and the Mo_3Sn phase overlap.¹⁶ The uncertainty in the values of x is about ± 0.02 .

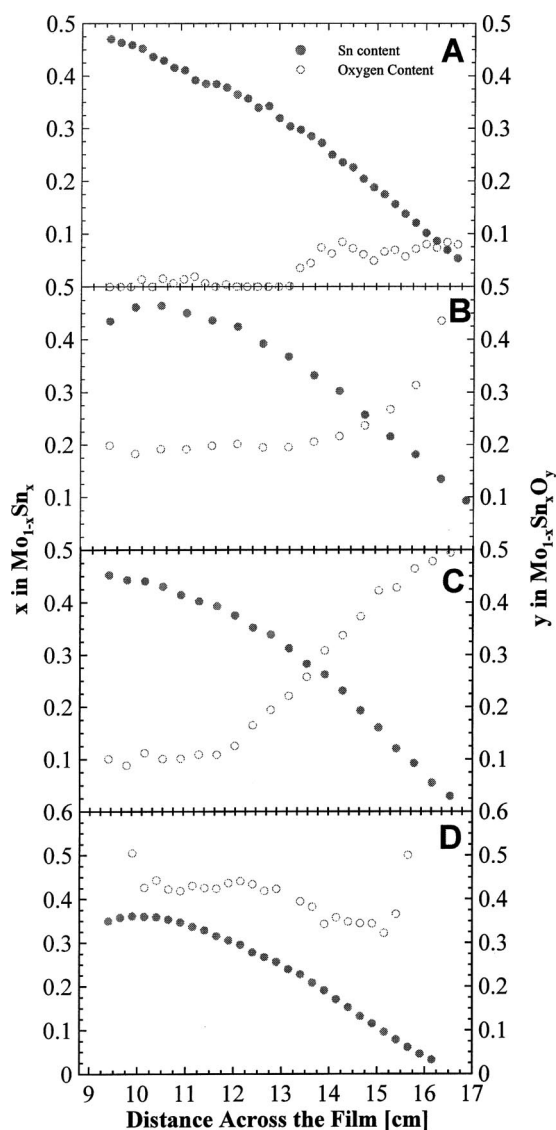


Figure 3. Sn (x in $\text{Mo}_{1-x}\text{Sn}_x$) and oxygen (y in $[\text{Mo}_{1-x}\text{Sn}_x]_{1-y}\text{O}_y$) compositions in films deposited on microscope slides at (A) 1.5 mTorr (SPE5), (B) 4 mTorr (SPD74), (C) 3.5 mTorr (Ar/O_2), and (D) 10 mTorr (SPD99) Ar pressure.

torial samples. The size of the X-ray beam spot on the specimen is about 1 by 1 mm.

For *in situ* XRD, a Siemens D5000 diffractometer equipped with $\text{Cu K}\alpha$ radiation and a diffracted beam monochromator was used. Each *in situ* X-ray scan took about 3 h and was collected in 0.05° increments between scattering angles of 20 and 50° . Every third scan was made between $20^\circ < 2\theta < 80^\circ$. For the experiment on nanostructured $\text{Mo}_{1-x}\text{Sn}_x$ with $x = 0.44$, three adjacent scans were binned together to improve the signal to noise ratio. Table II summarizes the crystal structure and composition of regions in each film.

The deposited mass was obtained by weighing the Cu disks before and after the deposition using a precision Cahn 29 microbalance with a 1×10^{-7} g resolution. An approximation of film thickness was made using the deposited mass and assuming an approximate density $\rho = (1 - x)\rho_{\text{Mo}} + x\rho_{\text{Sn}}$ with the nominal densities of $\rho_{\text{Mo}} = 10.2$ and $\rho_{\text{Sn}} = 7.3$ g/cm^3 . The active mass and thickness of the 1.3 cm diam electrodes varied from approximately 0.5 to 2 mg and from 0.5 to 1 μm from $x = 0.05$ to $x = 0.5$ in $\text{Mo}_{1-x}\text{Sn}_x$, respectively.

Table III. Summary of coin cell studies.

Sample	Average x in $\text{Mo}_{1-x}\text{Sn}_x$	Wt (mg)	Current (μA)	Voltage Range (V)	Experiment
SPD74	0.47	1.389	38	0-2.0	Discharge/charge
	0.45	1.216	29	"	"
	0.39	1.050	20	"	"
	0.31	0.927	13	"	"
SPD99	0.20	0.854	9	"	"
	0.08	0.836	4	"	"
	0.36	0.990	24	"	"
	0.33	1.036	23	"	"
SPE5	0.27	0.945	18	"	"
	0.19	0.847	13	"	"
	0.09	0.745	8	"	"
	0.42	1.878	45	0-2.0	"
SPE21	0.36	1.682	38	"	"
	0.29	1.472	29	"	"
	0.19	1.300	20	"	"
	0.08	1.132	12	"	"
SPF6	0.04	0.982	4	"	"
	0.49	2.206	53	0-1.2	"
	0.43	1.967	44	"	"
	0.38	1.733	34	"	"
SPF66A ^a	0.31	1.544	24	"	"
	0.22	1.328	14	"	"
	0.11	1.115	5	"	"
	0.30	0.931	15	0-1.5	"
SPF66C	0.30	0.908	10	"	"
	0.30	0.834	15	"	"
	0.30	0.889	10	"	"
	0.30	0.921	25	"	"
SPF66D ^a	0.30	0.838	25	"	"
	0.30	0.710	5	"	"
	0.46	2.313	23.4	0-1.2	"
	0.43	1.952	18.6	"	"
SPF66D ^a	0.38	1.677	14.2	"	"
	0.30	1.471	10	"	"
	0.18	1.339	5.6	"	"
	0.06	1.196	2	"	"
SPF66D ^a	0.46	2.335	25	"	GITT
	0.43	1.956	17.5	"	"
	0.38	1.677	15	"	"
	0.18	1.379	15	"	"
SPF66D ^a	0.06	1.290	7.5	"	"
	0.46	2.305	22.5	"	"
	0.46	0.3876	21	"	Discharge/charge
	0.45	0.3612	19	"	"
SPF66D ^a	0.44	0.3411	"	"	Shorted
	0.43	0.3188	15	"	"
	0.42	0.2946	14	"	"
	0.40	0.2754	12	"	"
SPF66D ^a	0.38	0.2558	11	"	Discharged/charged
	0.35	0.2507	"	"	Shorted
	0.32	0.236	9	"	Discharged/charged
	0.28	0.2444	8	"	"
SPF66D ^a	0.24	0.2362	6	"	"
	0.19	0.2252	5	"	"
	0.14	0.2262	5	"	"
	129A	0.44	2.00	22	0-2
129B	0.36	1.67	13	"	"
129C	0.22	1.34	6	"	"
SPG30	0.44	1.3	13	0-1.5	Discharged-charge
	0.40	1.2	10	"	"

^a SPF66A and SPF66D are 1.3 and 0.5 cm diam electrodes, respectively.

The width of the deposited region is 7.5 cm and the composition varied linearly across the width of the film. Therefore, the composition of the material sputtered on a single 1.3 cm diameter electrode varied somewhat with position. Error bars in the figures of this paper indicate this variation, whenever the composition is mentioned in

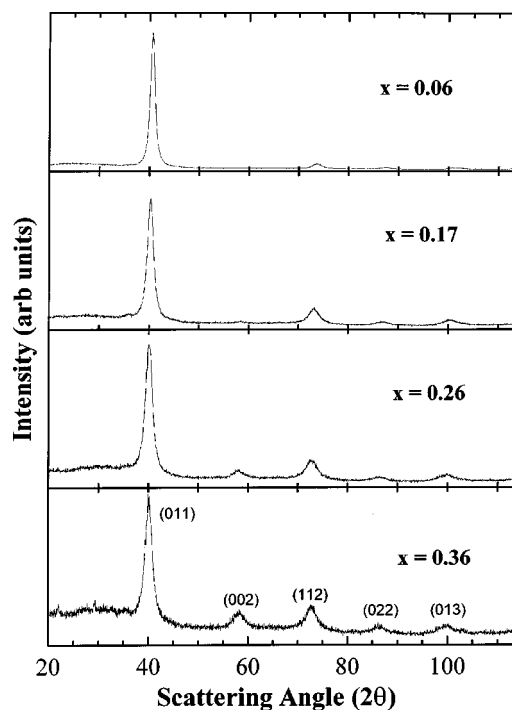


Figure 4. XRD patterns of film SPD99 for $0 < x < 0.36$, grown at 10 mTorr. The films show a BCC diffraction pattern. Very little Mo_3Sn is seen. The compositions, x , are indicated on the figure. As x decreases, (110) texturing increases.

the data. Some cells were made with 0.5 cm diam electrodes to reduce the compositional variation within the electrodes. However, those electrodes had a very small mass so that small currents that reach the accuracy and precision limits of our chargers ($\pm 2 \mu\text{A}$) were required. At least two coin cells for each average composition of each sputtering run were made.

The $\text{Mo}_{1-x}\text{Sn}_x$ films deposited on the Cu foils were used as positive electrodes vs. Li metal in 2325-type coin cells (23 mm diam, 2.5 mm thick). The cells were assembled in an argon-filled glove box. The electrodes were separated by Celgard 2502 membranes soaked with 1 M LiPF_6 in 33% ethylene carbonate/67% diethylcarbonate (v/v) (Mitsubishi Chemical) electrolyte. The cells were tested using constant charge/discharge currents between 0 and 1.5 V or between 0 and 2.0 V. The cells were discharged/charged at C/40 and C/20 rates, corresponding to a full theoretical limit of 4.4 Li per x in $\text{Mo}_{1-x}\text{Sn}_x$. A summary of all the cells studied in this work is given in Table III.

For *in situ* X-ray cells, Be discs (2.1 cm diam, 0.25 mm thickness) were used as substrates during the sputtering of Mo and Sn. The electrodes used had compositions of $x = 0.44 \pm 0.02$, 0.36 ± 0.03 , and 0.22 ± 0.05 and were prepared in sputtering run no. 129. The *in situ* cell hardware was the same as the standard 2325 hardware except that a hole in the cell can was made into which the coated Be disc was bonded. The discharge/charge currents were 22, 13, and $6 \mu\text{A}$ and the first discharge of three cells took 61, 40, and 30 h, respectively. The *in situ* measurements were made for three discharge/charge cycles and took about two weeks each.

Quasi-equilibrium voltage measurements were performed using the galvanostatic intermittent titration technique (GITT) using a Macpile II system for several compositions. Standard coin-type cells were constructed using 1.3 cm diam electrodes. The cells were discharged/charged for 0.5 h at a C/40 rate, then left on open circuit for 10 h or until $\Delta V/\Delta t < 1 \text{ mV/h}$, whichever condition was reached first. Then the sequence was repeated. The cell potential was recorded whenever it changed by 5 mV. All the coin cell details are given in Table III.

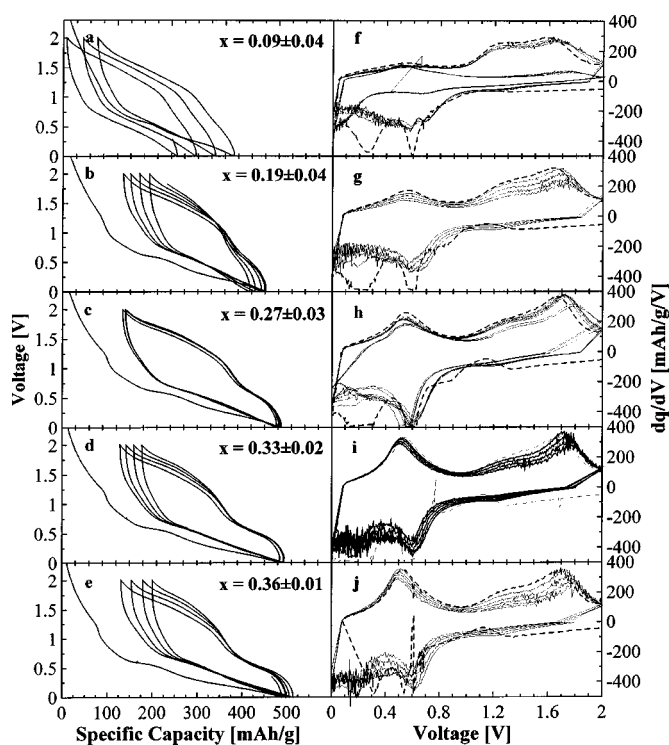


Figure 5. (a-e) Voltage vs. specific capacity for Li/[Mo_{1-x}Sn_x]_{0.6}O_{0.4} cells made from SPD99 containing about 40% oxygen. Four discharge/charge cycles are shown. (f-j) Differential capacity vs. potential (dq/dV vs. V) for the cells of Fig. 5a-e respectively.

Results and Discussion

Figure 1 shows the combinatorial mapping of Mo_{1-x}Sn_x for $0 < x < 1$ from the sputtering run SPD103 (Tables I and II). The entire compositional range of the binary system is mapped out in a single sputtering experiment. This experiment was made using two opposing linear deposition masks. Figure 2 shows XRD patterns collected at various points on the film. Various crystallographic regions of the film are clearly observed in Fig. 2 and described in Table II.

Previously we described the effect of growth conditions on formation of nanocrystalline BCC Mo_{1-x}Sn_x, crystalline BCC Mo_{1-x}Sn_x and Mo_{3+y}Sn phases.¹⁶ The BCC metals, generally exhibit a (110) orientation, because (110) planes are densely packed and this would lower the surface energy. We showed that metastable substitutional solid solutions of both BCC Mo_{1-x}Sn_x and β -tungsten structured Mo_{3+y}Sn are obtained by sputtering.¹⁶ Mo and Sn have no equilibrium solubility, however energetic sputtering and the rapid quench rates lead to these solid solutions.

The impact of Ar sputtering pressure on oxygen content in the resulting films is shown in Fig. 3. High-pressure depositions tend to grow more porous films, which are more susceptible to post-deposition oxidation.¹⁶ It is our opinion, based on the electrochemical results to be shown later, that the majority of this oxygen is bonded to molybdenum. It is essential to analyze for oxygen in such films because it has a large impact, as we will show. The measurements, when repeated on copper foil substrate, reveal similar amounts of oxygen as the measurements performed on glass substrate showing that the detected oxygen is from the film. Furthermore, no evidence of Si is seen in either analysis.

Oxygen-Containing Films

Figure 4 shows XRD results for sample SPD99, Mo_{1-x}Sn_xO_{0.4} ($0.02 < x < 0.36$). For large x , the samples show broad BCC peaks and the grains within the film exhibit random orientation be-

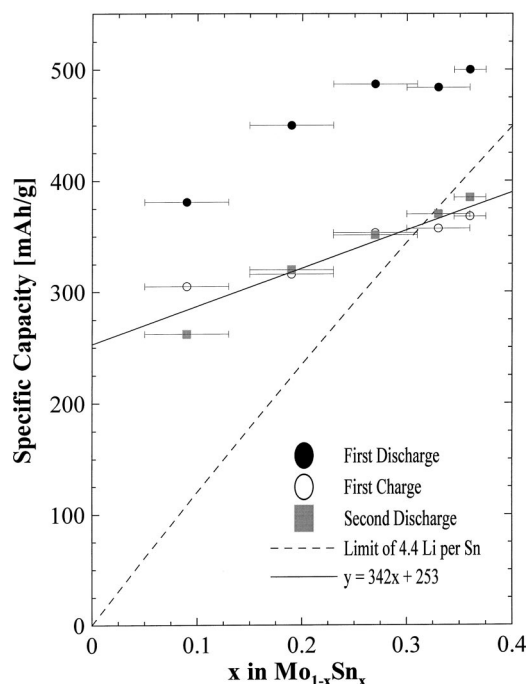


Figure 6. The first discharge, first charge, and second discharge capacities of Li/[Mo_{1-x}Sn_x]_{0.6}O_{0.4} cells plotted vs. x for sample SPD99 (40% oxygen). The capacity is mainly due to the reaction of Li with molybdenum oxide. The horizontal bars on the data points indicate an approximate range of the electrode composition.

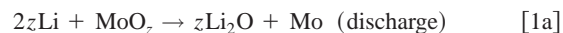
cause the Bragg peak intensities match those of a random powder. As x decreases the intensity of the (002) peak decreases strongly showing that the grains exhibit preferred orientation away from the (002) direction. The Bragg peaks shift smoothly to lower angle as x increases showing that the substitutional incorporation of Sn for Mo increases the cubic lattice constant.¹⁶

Figures 5a-e show the discharge/charge behavior of Li/Mo_{1-x}Sn_xO_y cells with different Sn contents, x . Each of the voltage-capacity profiles shown in figures 5a-e exhibits a region of high voltage capacity and a region of low voltage capacity during the charge (removing Li from the film). The capacity of the high voltage region is roughly constant as the Sn content varies but the low voltage capacity increases smoothly with Sn content.

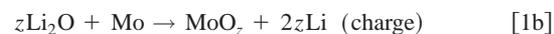
The details of the voltage profile can easily be amplified in differential capacity vs. potential (dq/dV vs. V) plots (Fig. 5f-j). The two capacity regions observed in Fig. 5a-e are easily discerned in figures 5f-j. For the charge, one region is centered around 0.5 V and the other spans the range between 1.2 and 2 V. The 1.2-2 V charge capacity or the area under the dq/dV curve in the 1.2-2 V range, remains almost constant for different values of x , whereas the 0.5 V charge capacity increases as x increases.

The portion of the capacity that is independent of the Sn content is probably due to the reaction of Li with molybdenum oxide, MoO_y, via a displacement reaction, where Li₂O and MoO_y would form during discharge (adding Li) and charge (removing Li), respectively. This high voltage capacity during charge is absent in films that contain little oxygen as we show later. The capacity due to MoO_y remains constant since there is an approximately constant amount of oxygen in all the cells made from the SPD99 film.

Metal oxides such as molybdenum oxide typically show large hysteresis between the potentials for the reactions



and



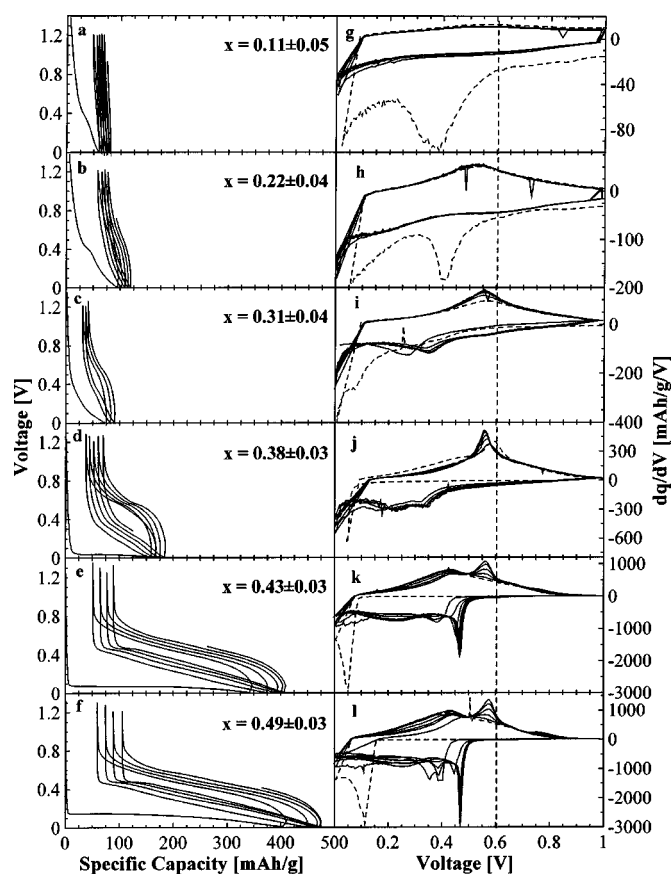


Figure 7. (a-f) Voltage vs. specific capacity of Li/Mo_{1-x}Sn_x cells made from sample SPE21 containing negligible (<5%) oxygen content. Five discharge/charge cycles are shown. The rightward shifts in the discharge/charge curves are due to a charge/discharge current imbalance. (g-l) Differential capacity vs. potential (dq/dV vs. V) for the same cells in Fig. 7a-f. The first cycle is drawn dashed. Notice the emergence and growth of a peak at 0.58 V for $x = 0.43$ and $x = 0.49$.

Similar displacement reactions have been proposed in the case of other metals oxides like CoO and FeO.^{17,18} During the process of equation 1a, the cell potential apparently overlaps that of the Li/Mo-Sn reaction. However, during charge the Li/Mo-Sn (centered at 0.5 V) reaction and the reaction described by Eq. 1b are easily separated. The reaction of Li with Mo-Sn also contributes to the capacity in Fig. 5. This is why the capacity of the plateau centered at 0.5 V in Fig. 5a-e and the peak centered at 0.5 V in Fig. 5f-j increase in strength as x increases.

Figure 6 summarizes the capacity observed in the cells made from the SPD99 film as a function of Sn content. A material with an overall stoichiometry of Mo_{0.6}O_{0.4} reacting via Eq. 1a would have a theoretical capacity of 335 mAh/g. If the data points for the first charge and second discharge are extrapolated back to $x = 0$ (which would correspond to about Mo_{0.6}Sn_{0.4} by Fig. 3b), one obtains a reversible specific capacity of about 250 mAh/g which is in fair agreement with the estimate for Mo_{0.6}O_{0.4}. If the first discharge capacity is extrapolated back to $x = 0$, then a capacity of about 300 mAh/g is obtained. In any event, it is clear that the Reactions 1a and 1b are occurring in these oxygen-containing films.

The slope of the line drawn through the data points for the first charge and second discharge of Fig. 6 is about 340 mAh/g per $x = 1$. This suggests that each Sn atom in the BCC Mo_{1-x}Sn_x phase can react with about 1.5 Li atoms. We will see that this agrees well with values determined for the pure (no oxygen) BCC Mo_{1-x}Sn_x phase.

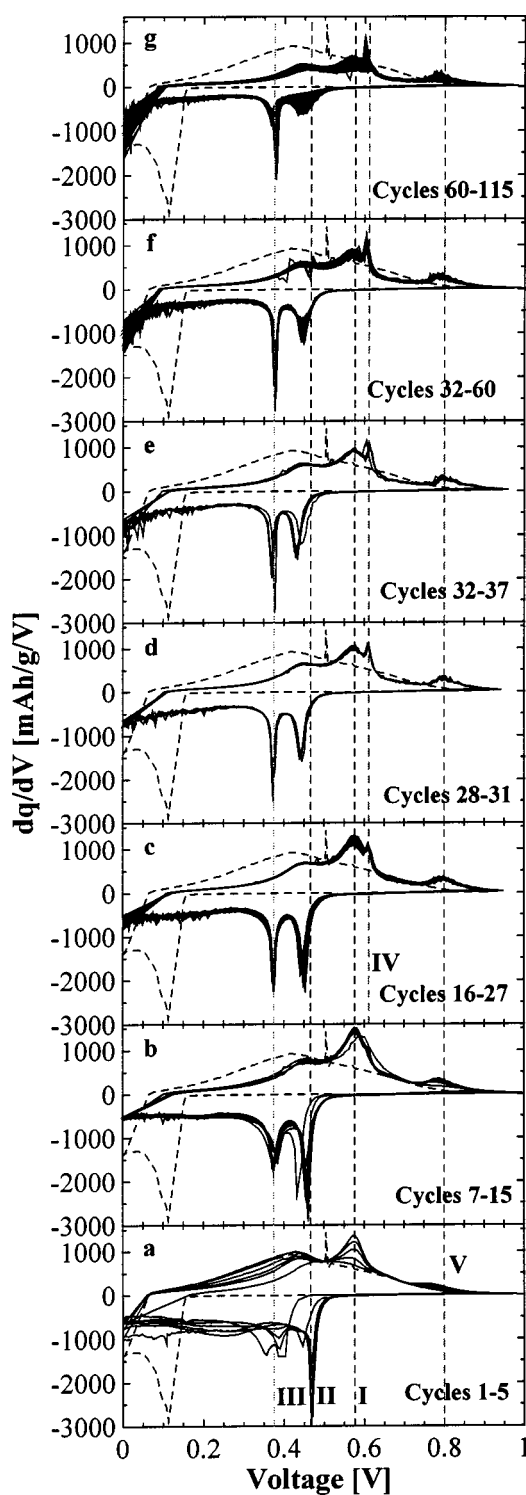


Figure 8. The differential capacity vs. potential (dq/dV vs. V) for the first 115 cycles of the cell described by Fig. 7f and l. The cell electrode was from film (SPE21) with $x = 0.49$ in Mo_{1-x}Sn_x. During the charging regime, peak I (0.58 V) grows, and peak IV appears after about 30 cycles and slightly moves to right. During the discharge, peak II (0.46 V) shrinks and moves to the left, whereas peak III (0.35 V) grows. The dotted line represents the first discharge/charge cycle.

Films Containing Little Oxygen

Figure 2 shows typical diffraction patterns for a sample (SPD103) sputtered under low argon pressure conditions that does not uptake substantial oxygen. Diffraction patterns for films SPE5,

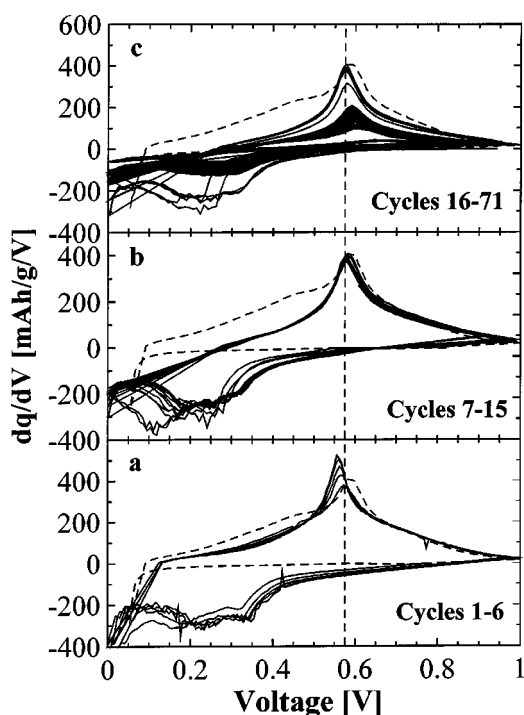


Figure 9. The differential capacity vs. potential (dq/dV vs. V) for the first 71 cycles of the cell described by Fig. 7d and j. The cell electrode was from film (SPE21) with $x = 0.038$ in $\text{Mo}_{1-x}\text{Sn}_x$. No new peaks emerge. The gradual reduction in the peak areas reflects the loss of capacity during cycling.

SPE21 and SPF66 are basically identical to those shown for the same compositions. In all cases the films give a set of sharp diffraction peaks for $x < 0.35$ that can be indexed on a BCC structure. For compositions between about $0.11 < x < 0.31$, a second set of peaks is observed, corresponding to a Mo_{3+x}Sn phase. For compositions above $x > 0.37$, broad diffraction peaks are observed that are caused by coexisting nanoscopic grains of $\text{Mo}_{0.63}\text{Sn}_{0.37}$ and nanoscopic regions of Sn atoms that cannot be accommodated in the saturated BCC phase.⁹ Many films were prepared so that the reproducibility of film structure and electrochemical behavior could be assured.

The first five discharge/charge cycles of $\text{Li}/\text{Mo}_{1-x}\text{Sn}_x$ cells prepared from electrodes with a minimal amount of oxygen ($<5\%$) are shown in Fig. 7a-f. The voltage profiles of the high Sn content cells are characterized by a low voltage plateau (0.1 V) during the first discharge capacity, which dramatically differs from subsequent discharge or charge cycles. As x in $\text{Mo}_{1-x}\text{Sn}_x$ increases, the first discharge capacity and the reversible capacity becomes larger. The samples with $x < 0.35$ that are crystalline phases have relatively small reversible capacities. On the other hand, the nanostructured materials ($x > 0.38$) show about 350 mA h/g reversible capacity.

Figures 7g-l show the differential capacity vs. voltage for the first five cycles of the cells described by Fig. 7a-f. The dashed curves in Fig. 7g-l represent the first discharge/charge cycle. The nanocrystalline materials ($x > 0.38$) show changes to several dq/dV peaks during charge/discharge cycling. There is a peak growing near 0.55 V during charge, and changes in the discharge peaks around 0.37 and 0.47 V are seen. On the other hand, the predominantly crystalline phases ($x < 0.38$) do not show any significant change in their dq/dV plots with cycling.

The progression of dq/dV vs. V as a function of cycle number for the $x = 0.49$ and the $x = 0.38$ samples are shown in Fig. 8 and 9, respectively. $\text{Mo}_{0.51}\text{Sn}_{0.49}$ shows a number of changes in the dq/dV profile as it cycles 115 times. The first charge (removing Li)

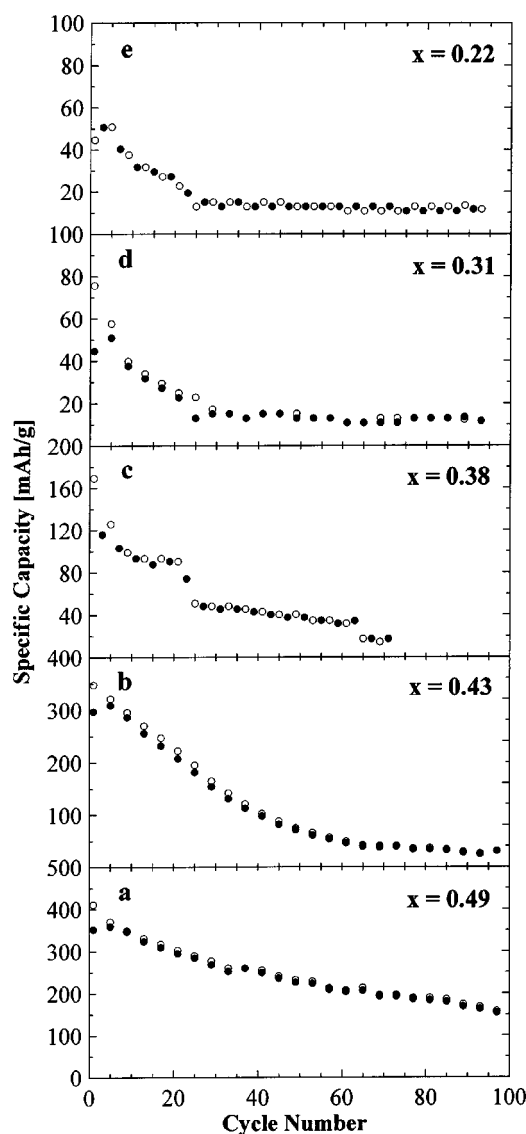


Figure 10. (a-e) Capacity vs. cycle number for the cells of Fig. 7b-f. The electrodes were from film SPE21. Open and filled circles denote discharge and charge, respectively.

shows a very broad peak at about 0.4 V. During the subsequent charge processes, a peak near 0.58 V appears and grows until the 15th cycle. After the 15th cycle, the 0.58 V peak diminishes and a very sharp and small peak around 0.62 V keeps growing until the 60th cycle. A small broad peak also appears at 0.8 V after the first few cycles. Over the first five cycles, the initial sharp peak at 0.47 V during discharge (adding Li) moves to the left and shrinks in size, and is replaced by a peak around 0.35 V. After 60th cycle all peaks in discharge and charge shrink, which corresponds to a decrease in the total capacity.

Previously, dq/dV curves have been used to study the formation of Li-Sn alloy phases in $\text{SnO}:x\text{B}_2\text{O}_3:y\text{P}_2\text{O}_5$ composite glasses.¹⁹ The changes to the dq/dV vs. V profiles of nanocrystalline $\text{Mo}_{1-x}\text{Sn}_x$ as a function of cycle number are very similar to those of SnO glass composites. In particular, $\text{SnO}:0.1\text{B}_2\text{O}_3:0.1\text{P}_2\text{O}_5$ also shows a growth in the 0.6 V peak during charge, a decrease in 0.45 V peak during discharge and a growth of a 0.35 V peak during discharge as cycle number increases. Courtney *et al.* have argued that these new peaks are caused by the aggregation of Sn atoms into clusters in the amorphous glass matrix.²⁰ The growth and sharpening of the peaks is caused by an increase in the size of the Sn clusters.

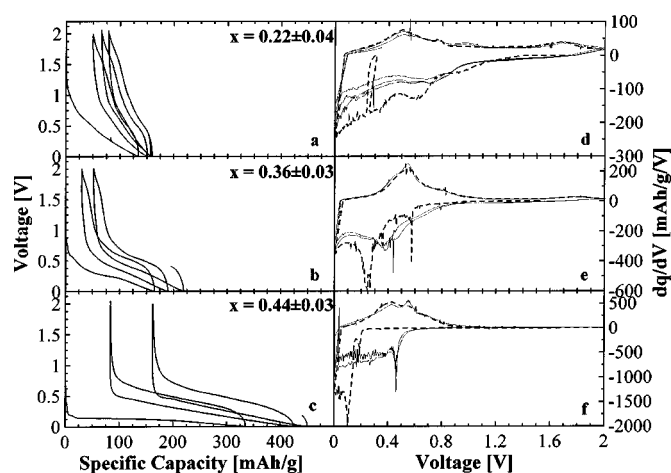


Figure 11. (a-c) Voltage vs. specific capacity for the Li/Mo_{1-x}Sn_x cells used in the *in situ* X-ray studies. The electrodes were from film no. 121. (d-f) Differential capacity vs. potential (dq/dV vs. V) for the same cells.

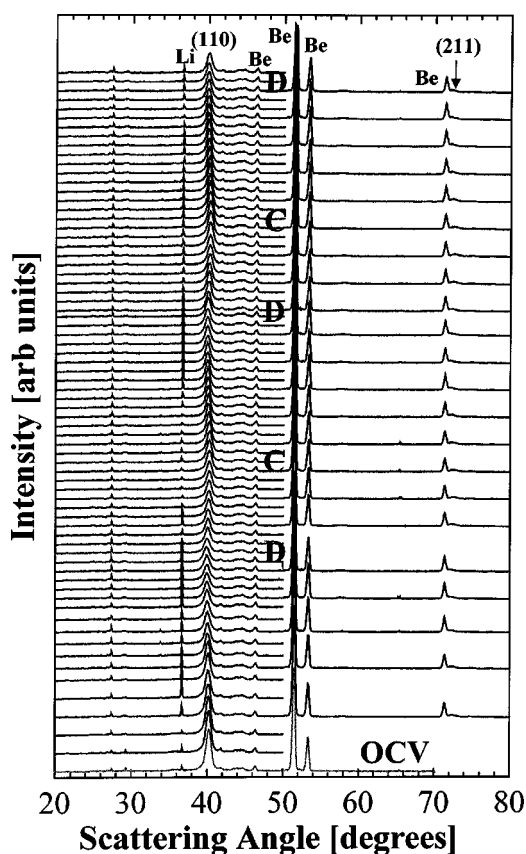


Figure 12. The XRD patterns taken during the charge and discharge of the Li/Mo_{1-x}Sn_x *in situ* cell with $x = 0.36$. The BCC Miller indices, (110) and (211), are labeled. The smooth variations in the Bragg angle of the dominant (110) peak are clearly visible. No other peaks appear during the charge and discharge regimes. C and D denote the end of charge and discharge processes, respectively.

The changes in the peak positions during discharge were speculated to be caused by changes in the stable phases of Li-Sn alloys as Sn clusters change their size. Similar behavior is thought to be occurring here. During the initial cycles, Sn clusters grow until they reach a steady state. Meanwhile changes in the peak position are probably

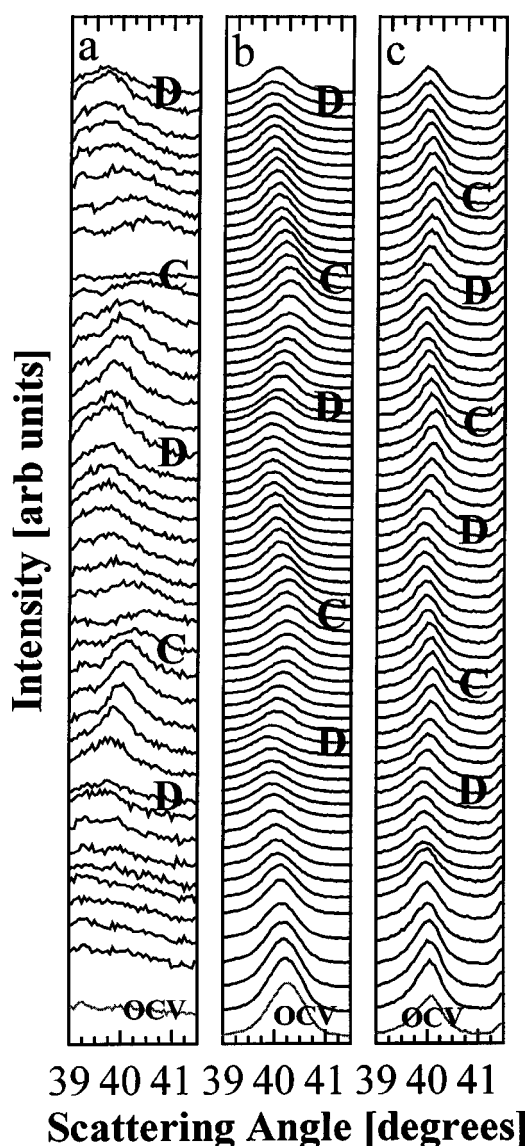


Figure 13. The (110) diffraction peak for the $x = 0.44$ (a), $x = 0.36$ (b), $x = 0.22$ (c) samples during the discharge/charge process. The crystalline peaks (b,c) show smooth variations during the discharge and charge regimes. The nanocrystalline peak for Mo_{0.56}Sn_{0.44} (a) also shows a variation in its position. C and D denote charged and discharged states, respectively.

due to changes in the Li-Sn phases that have different stability for a given cluster size.

Figure 9 shows that the crystalline Mo_{1-x}Sn_x ($x < 0.4$) electrodes behave differently. The differential capacity vs. voltage for a Li/Mo_{0.62}Sn_{0.38} cell as a function of cycle number exhibits no significant change. The absence of new peaks indicates that Sn does not aggregate out of the BCC structure and that Li-Sn phases do not form during the Li insertion and/or removal. This is a first indication that a topotactic Li insertion process occurs in the BCC phase Mo_{1-x}Sn_x material. *In situ* XRD results were used to confirm this hypothesis.

Figure 10 shows the specific capacity vs. cycle number for the same cells that are described by Fig. 8 and 9. Each of the cells shows significant capacity loss with cycle number. The capacity drop at cycle 20 for the cell with $x = 0.38$ was caused by an increase in the cycling current but up to this point the cell was performing well.

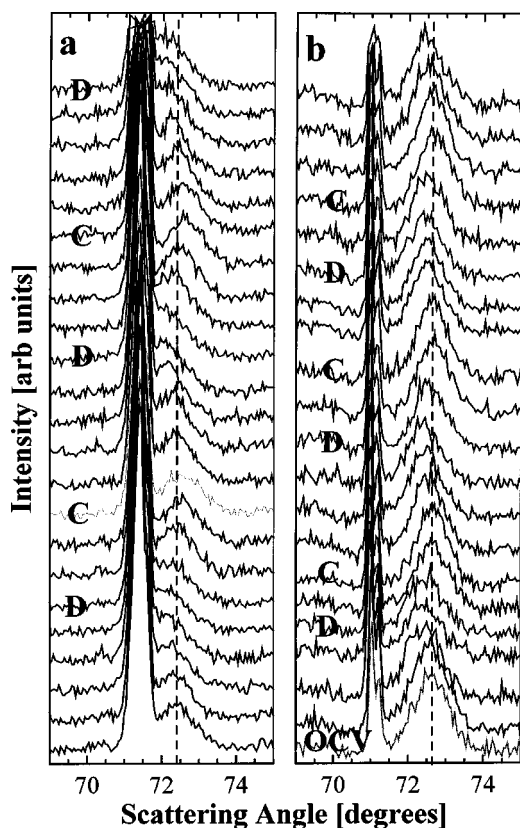


Figure 14. The (211) diffraction peak for the (a) $x = 0.36$ and (b) $x = 0.22$ samples during the discharge/charge process. The peaks show periodic shifts in Bragg angle during the discharge and charge. The intense sharp peak is from the Be window on the cell. C and D denote end of charge and discharge processes, respectively.

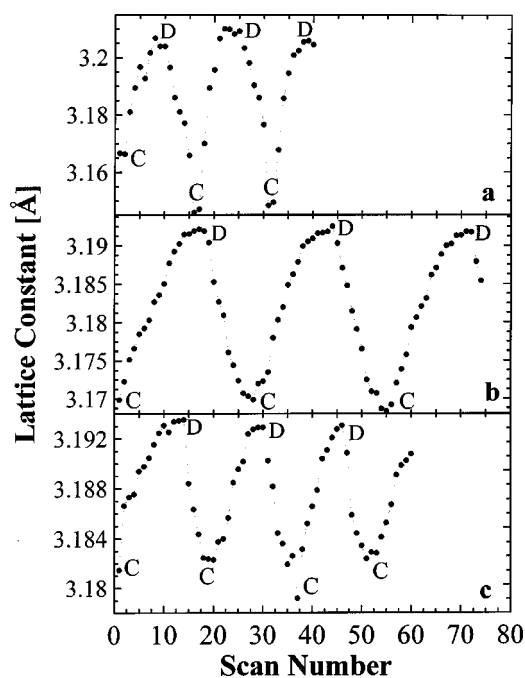


Figure 15. Periodic oscillations of the BCC $\text{Mo}_{1-x}\text{Sn}_x$ lattice constant during the discharge/charge cycling for the $x = 0.44$ (a), $x = 0.36$ (b), and $x = 0.22$ (c) samples. C and D denote the end of charge and discharge processes, respectively.

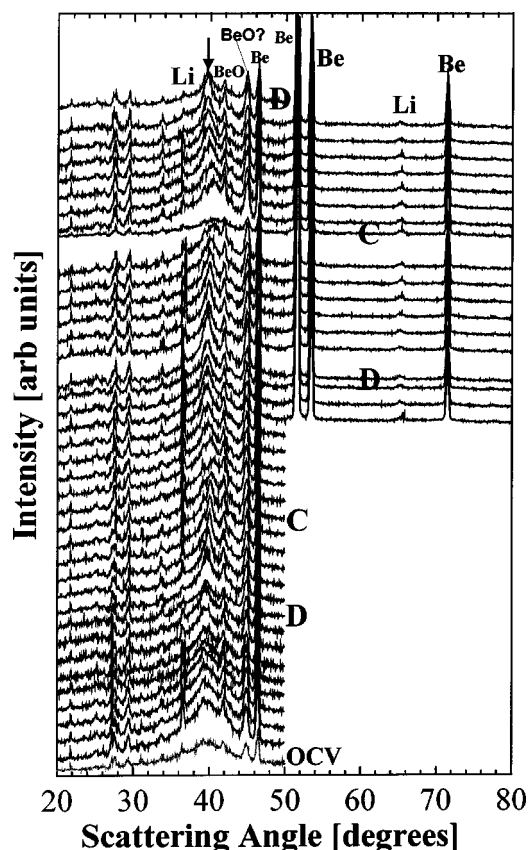


Figure 16. The XRD patterns taken during the charge and discharge of the $\text{Li}/\text{Mo}_{1-x}\text{Sn}_x$ *in situ* cell with $x = 0.44$. The (110) peak region is indicated by a heavy arrow. Variations in the Bragg angle of the dominant (110) peak are clearly visible. No other peaks appear during the charge and discharge regimes. C and D denote the end of charge and discharge processes, respectively. Peaks due to the cell holder are indicated.

In situ XRD experiments were performed for samples from film no 129 with compositions $x = 0.22 \pm 0.04$, 0.36 ± 0.03 , and 0.44 ± 0.03 . Figure 11 shows the voltage vs. specific capacity and the differential capacity vs. potential for these *in situ* XRD cells. The results in Fig. 11 match well with the results for standard coin cells in Fig. 7. As in Fig. 7, the nanocrystalline $x = 0.44$ sample shows an emerging peak in dq/dV around 0.6 V during the second charge cycle whereas the crystalline samples give differential capacity data that do not change significantly with cycle number. The data in Fig. 11 are noisier than the results in Fig. 7 because the *in situ* XRD cells are not temperature controlled during cycling in the diffractometer.

Figure 12 shows the *in situ* XRD scans for the $x = 0.36$ sample. The scans corresponding to full discharge (D) and charge (C) are indicated. During the first discharge, the (110) peak intensity decreased and the peak shifted to smaller angle due to lattice expansion. The film initially exhibited (110) preferential orientation that is apparently reduced during the first discharge. The corresponding shifting of the (211) peak can also be observed by referencing its position to the neighboring peak from the Be window. During the subsequent charge and discharge cycles both the (110) and (211) peaks shift reversibly. No new peaks indicative of other phases are observed.

The behavior of the sample with $x = 0.22$ is very similar, except that the shifts of the (110) and (211) peaks due to topotactic Li insertion are smaller than for the $x = 0.36$ sample because the amount of Li that can be accommodated is smaller. Figures 13 and 14 show expanded views of the (110) and (211) peak regions for the $x = 0.36$ and $x = 0.22$ samples. Figures 13b and c show the revers-

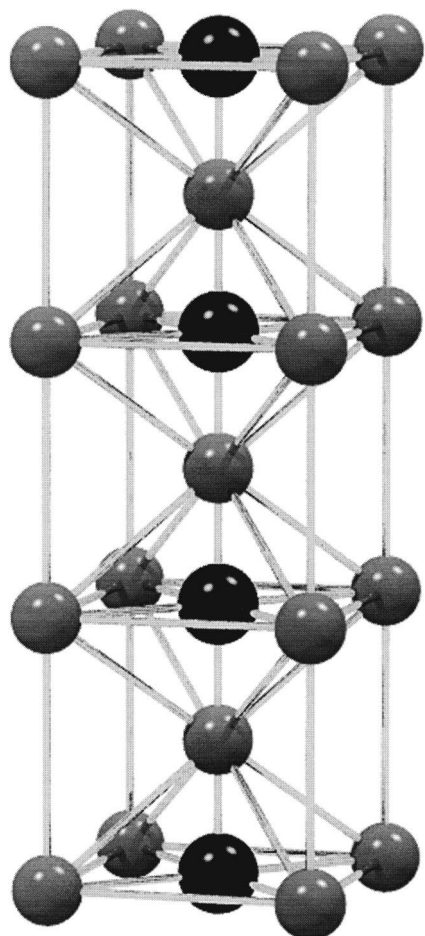


Figure 17. The BCC lattice where Mo and Sn atoms randomly occupy the body centers and corners of the cube. Darker spheres in the octahedral sites designate possible locations for inserted Li atoms.

ible shifting of the (110) peak for the $x = 0.36$ and $x = 0.22$ samples respectively. Figures 14a and b show the reversible shifting of the (211) peak for the $x = 0.36$ and $x = 0.22$ samples, respectively.

The lattice constants of the BCC phase as a function of Li content were obtained from the (110) scattering angle using the Bragg law and are shown as a function of the X-ray scan number in Fig. 15b and c for the $x = 0.36$ and $x = 0.22$ samples. The oscillations in the lattice parameter are periodic and show that the BCC lattice expands/shrinks during Li insertion/removal. We take this as definite evidence for the topotactic insertion of Li into interstitial sites of BCC $\text{Mo}_{1-x}\text{Sn}_x$. There is some off-axis displacement of the electrode with respect to the goniometer center so the exact values of the lattice parameters may be systematically off, because higher Sn content samples have larger lattice constant.¹⁵ However, the changes of the lattice constants with state-of-charge are considered accurate.

In situ XRD studies were also made on the $x = 0.44$ sample from film no. 129. This material is initially nanocrystalline and shows a diffraction pattern much like that in Fig. 2 for the $x = 0.51$ sample. Figure 16 shows the changes to the diffraction pattern that occur as the $\text{Li}/\text{Mo}_{0.56}\text{Sn}_{0.44}$ cell is sequentially discharged and charged. Since the electrode is nanocrystalline the Bragg peaks from the electrode material are broad and we had to magnify the intensity scale to observe them. This means that weak peaks from cell parts below 30° that were difficult to observe in Fig. 12, are more easily observed here. Furthermore the changes to the diffraction pattern are much harder to interpret. Figure 13a shows the position (110) peak region as a function of state of charge. Figure 15a

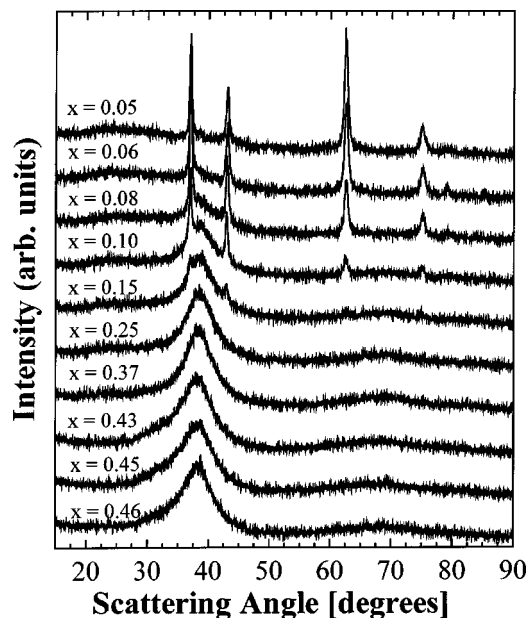


Figure 18. XRD patterns as a function of composition for film SPD74 from $x = 0.46$ in $\text{Mo}_{1-x}\text{Sn}_x$ (bottom) to $x = 0.05$ (top). The sample is nanocrystalline in the range $0.10 < x < 0.4$. For $x \leq 0.10$, a crystalline face centered cubic phase, presumably a molybdenum suboxide is observed.

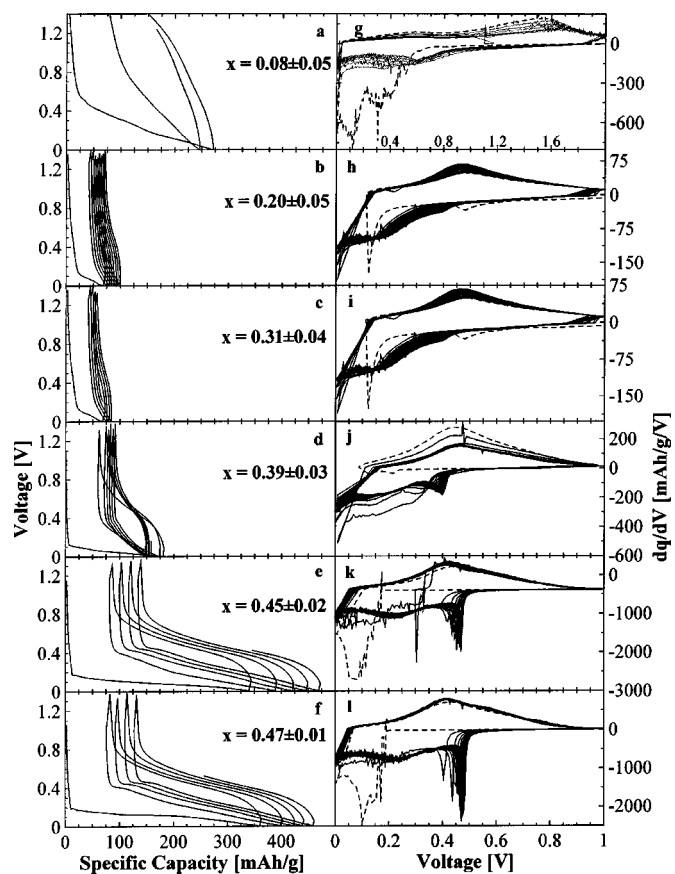


Figure 19. (a-f) Voltage vs. specific capacity for $\text{Li}/[\text{Mo}_{1-x}\text{Sn}_x]_{1-y}\text{O}_y$ cells of sample SPD74. The high voltage capacity of (a) is due to presence of high oxygen concentration (40%) in the sample. (g-l) Differential capacity vs. potential (dq/dV vs. V) profiles of the same cells.

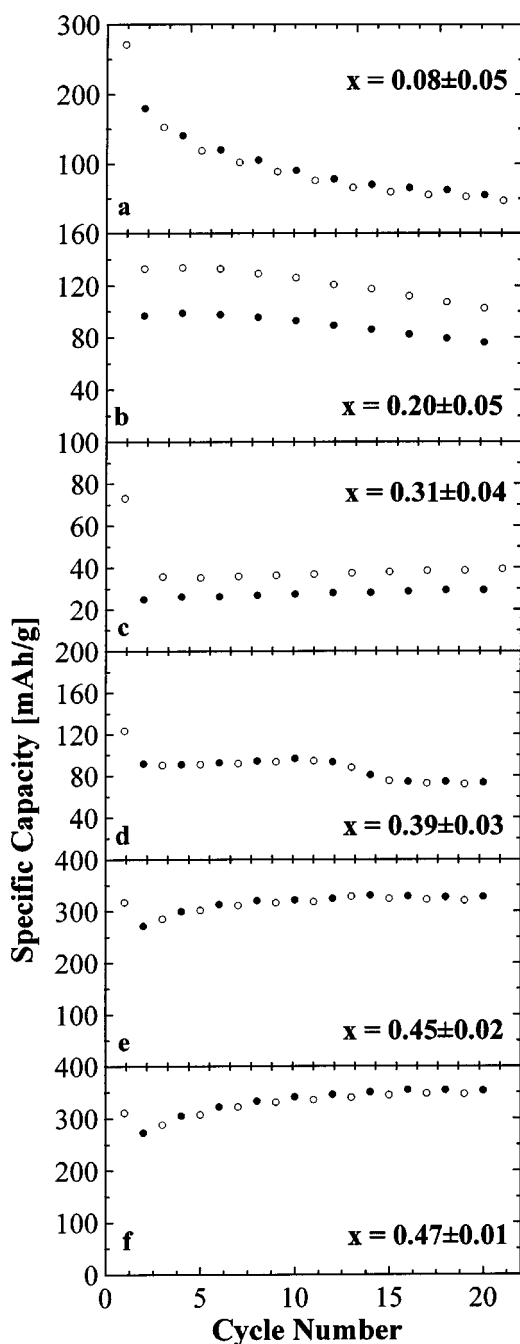


Figure 20. Capacity vs. cycle number for the cells described by Fig. 19. Open and filled circles denote discharge and charge, respectively.

shows the lattice constant derived from the (110) peak position plotted vs. X-ray scan number with the positions of full discharge and charge indicated. Again, there appear to be reversible changes to the lattice.

Based on the results in Fig. 13, 14, 15, and 16, we assume that reversible topotactic insertion of Li into interstitial sites is occurring in these BCC $\text{Mo}_{1-x}\text{Sn}_x$ samples. What are the interstitial sites that might be involved? The octahedral sites located at the center of the faces of the conventional BCC unit cell (Fig. 17) are possible interstitial sites for Li atoms. Hydrogen has shown to insert in the interstitial sites of BCC metals like Nb. Alpha-NbH contains two hydrogen atoms per BCC subcell tetrahedrally bonded to Nb.²⁰

The nanocrystalline materials are certainly more complex to interpret than the crystalline BCC phases. As shown before, the

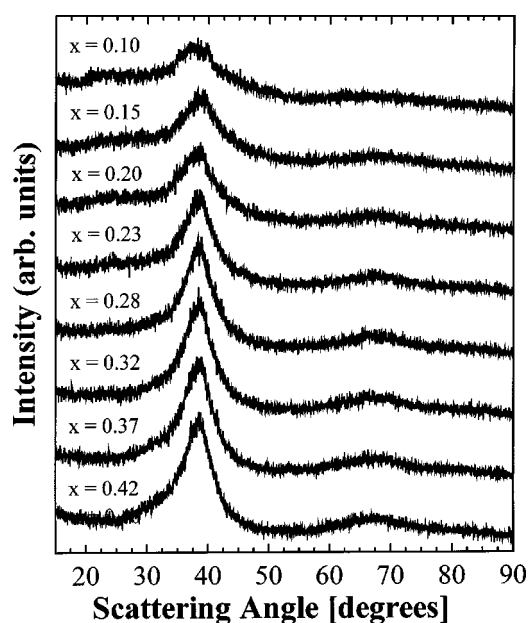


Figure 21. XRD patterns as a function of composition for film SPG30 from $x = 0.42$ in $\text{Mo}_{1-x}\text{Sn}_x$ (bottom) to $x = 0.1$ (top). The sample is nanocrystalline in the entire range.

dq/dV patterns show aggregation of Sn into larger clusters with cycle number, however *in situ* XRD patterns for the $x = 0.44$ sample show no new peaks in the first three cycles. X-ray studies of electrodes cycled for tens of cycles are needed to help understand the changes to the electrode structure with cycling.

Film SPD74, SPG30

The best cycling performance for all the samples we have studied were found in film SPD74. Figure 18 shows the diffraction patterns taken as a function of position along film SPD74. For all compositions above $x = 0.1$ in $\text{Mo}_{1-x}\text{Sn}_x$ the film shows a nanocrystalline pattern, which does not agree with what we have found in the range $0.1 < x < 0.38$ for other films. In addition, for $x < 0.1$, a surprising diffraction pattern is observed that can be indexed on a face centered cubic (FCC) lattice with $a = 4.15 \text{ \AA}$. Pure molybdenum does not exhibit a FCC phase.

Based on the results of Fig. 3b that show this film contains oxygen, we believe that the SPD74 film has had some oxygen incorporated during sputtering, not only during postdeposition oxidation. There are reports in the literature of a substoichiometric molybdenum oxide, Mo_3O that has an FCC structure.²¹ Presumably the sput-

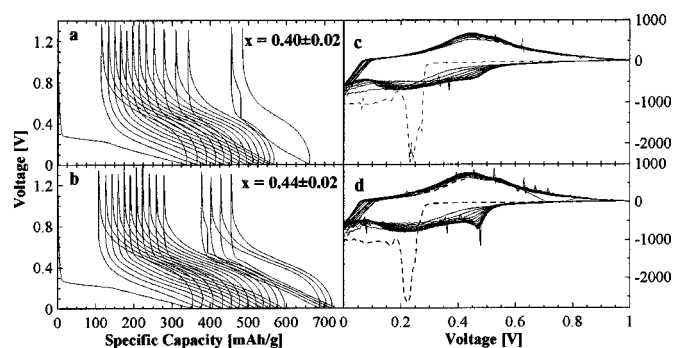


Figure 22. (a-b) Voltage vs. specific capacity for $\text{Li}/[\text{Mo}_{1-x}\text{Sn}_x]_{1-y}\text{O}_y$ cells of sample SPG30. (c-d) Differential capacity vs. potential (dq/dV vs. V) profiles of the same cells.

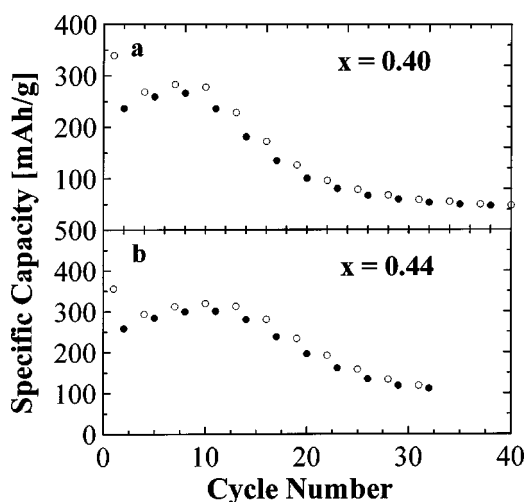


Figure 23. Capacity vs. cycle number for the cells described by Fig. 22.

tering was made under conditions involving a small leak of air or of target cooling water and this has led to this material. Apparently, according to this hypothesis, the incorporated oxygen also disturbs the formation of the crystalline BCC phase for $x > 0.1$, and nanocrystalline materials are formed. A close examination of Fig. 18 shows the growth of a shoulder near 31° as x increases above 0.4. This shoulder is due to diffraction from nanoscopic Sn that cannot be incorporated in the solid-solution phase. We believe that all the compositions in film SPD74 contain some incorporated oxygen.

Figure 19 shows the charge/discharge behavior of cells containing the SPD74 films. All these cells with nanocrystalline grains show smooth dq/dV vs. V curves with no emerging peaks during the entire 20 cycles, even for $x > 0.4$. Figure 20 shows the capacity vs. cycle number for the same cells. Most interesting are the results for $x = 0.45$ and $x = 0.47$. The cells with these electrodes show small irreversible capacity, little capacity loss over 20 cycles and specific capacities near 350 mAh/g.

We believe that presence of 20% oxygen in the SPD74 film has helped to stabilize the nanocrystalline structure against Sn aggregation and the subsequent formation of LiSn phases, which would normally limit the cycling capability of the material. In the case of SnO glass composites, it has been shown that more glass ($B_2O_3:P_2O_5$) in the composite retards the clustering of Sn and helps to improve the cycling life. It has also been suggested that capacity fade can be avoided if Sn particles are imbedded in a reduced matrix MoO_x , where $x < 1$.²²

To investigate the effect of oxygen during the growth, a deposition experiment (SPG30) with similar sputtering conditions to run SPD74 was performed. In this run, gas flows of 3.5 standard cubic centimeters per minute (sccm) of argon, and 0.5 sccm of oxygen were used. The total pressure was about 3.5 mTorr. The oxygen concentration in the film increases from about 10% at the Sn-rich end of the film to about 50% in the Mo end (Fig. 3c). The X-ray patterns of the film indicate the nanocrystalline structure throughout the composition range of $0.02 < x < 0.44$ (Fig. 21). Thus we were able to approximately reproduce the structure and composition of the Mo-Sn films made in run SPD74.

The voltage-capacity and differential capacity-potential profiles of the (SPG30) films are shown in Fig. 22 for $x = 0.40$ and $x = 0.44$. These are the interesting compositions because lower Sn content films have lower capacities, and higher irreversible capacities. As was the case in the oxygen-containing nanocrystalline SPD74 cells, the SPG30 cells show almost no formation of Sn clusters. The differential capacity profiles of the SPG30 samples with $x = 0.40$ and $x = 0.44$ are very similar to those of SPD74: no significant 0.6 and 0.35 V peaks appear during charge and discharge,

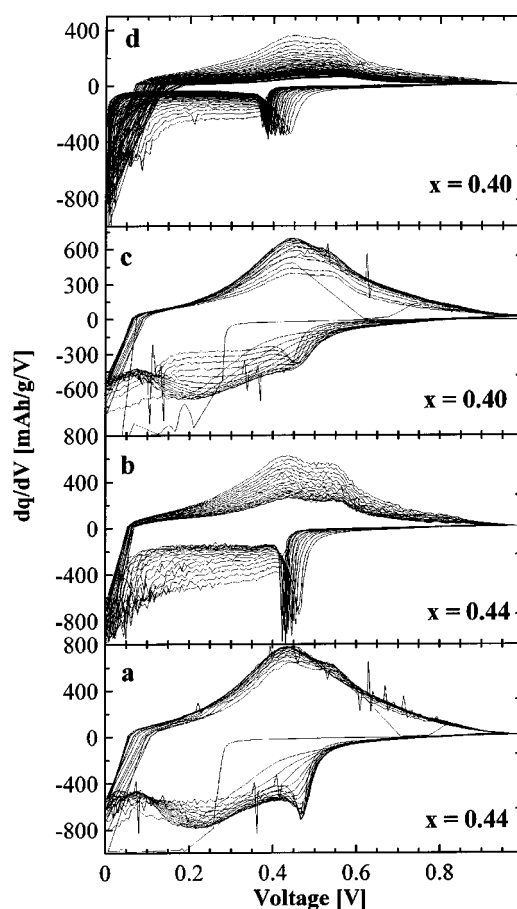


Figure 24. (a,c) Differential capacity vs. potential (dq/dV vs. V) of the SPG30 cells with $x = 0.44$ and $x = 0.40$ for the first 15 cycles. The growth of the 0.6 V peak during charge is significantly retarded. No peak around 0.35 V appears during discharge. (b,d) Further cycles show a dramatic reduction in the capacity due to poor adhesion at the film/substrate interface.

respectively. However, the capacity retention for these samples is relatively poor (Fig. 23). The initial increase in the capacity during the first few cycles is attributed cracking of the film. During cracking, new surfaces are presumably exposed, allowing better access of the Li ions to the electrode. After about 15 cycles a rapid loss in capacity is observed. A closer look at the differential capacity vs. potential for the $x = 0.40$ and $x = 0.44$ samples reveals only a slight growth of a 0.6 V peak during the charge (Fig. 24). We believe that for these cells, the loss in capacity is due to the delamination of the film from the substrate during repeated cycling. An inspection of the cells after 50 cycles showed that almost all of the film had delaminated from the copper substrate.

It is clear that the presence of oxygen in the SPD74 and SPG30 films has a dramatic effect on the rate of aggregation of Sn into larger clusters. It is our opinion that this effect deserves further study.

Summary of Specific Capacity vs. x in $Mo_{1-x}Sn_x$ for All Films Except SPD99

Figure 25 shows the specific capacity plotted vs. x in $Mo_{1-x}Sn_x$ for the first discharge (Fig. 25a), first charge (Fig. 25b) and second discharge (Fig. 25c) of Li/ $Mo_{1-x}Sn_x$ cells. All of the films except SPD99, that had large oxygen content due to postdeposition oxidation, have been included. The dashed line in each panel shows the specific capacity that would have been attained if each Sn atom had reacted with 4.2 Li atoms. The bold arrows in the figures indicate

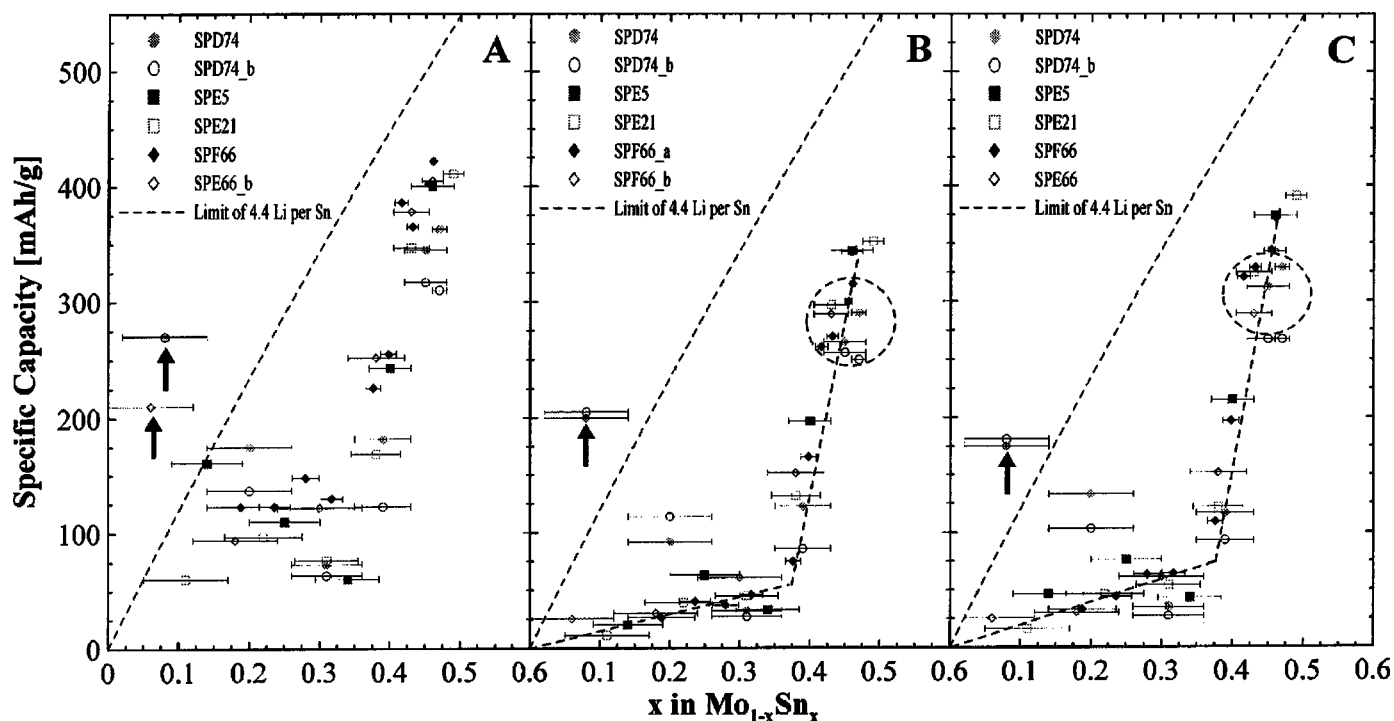


Figure 25. First (a) discharge, first charge (b), and second discharge (c) specific capacity vs. x in $\text{Mo}_{1-x}\text{Sn}_x$ shown for large number of $\text{Li}/\text{Mo}_{1-x}\text{Sn}_x$ cells. The data labeled SPF66_a was collected in coin cells using 0.5 cm diam electrodes, and the rest were collected using 1.3 cm diameter electrodes. The horizontal bars on the data points indicate an approximate range for the electrode composition. In b and c, the dashed lines through the data are drawn as guides to the eye. The circled regions show an optimum region for further studies and the dark arrows indicate cells with 40% oxygen content.

those samples that had oxygen contents greater than 20% (the samples with $x < 0.15$ in SPD74), and hence larger than expected capacity.

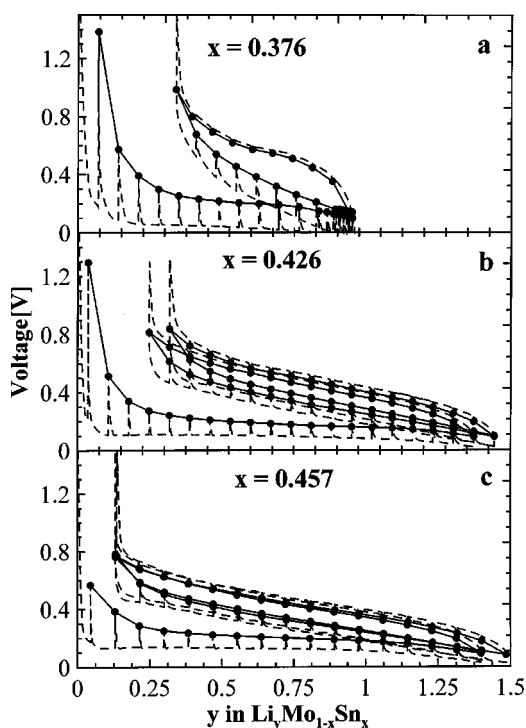


Figure 26. Voltage vs. y in $\text{Li}_y\text{Mo}_{1-x}\text{Sn}_x$ results of GITT experiments shown for several compositions. Filled circles show the voltages attained after relaxation, whereas voltages under load are shown with dashed lines.

Most striking about Fig. 25 is the clear change in slope of the specific capacity vs. x graphs around $x = 0.36$ as indicated by the guides to the eye in panels b and c. This is exactly the composition of the limit of the BCC phase; beyond $x = 0.36$, the BCC phase coexists with nanocrystalline Sn (Fig. 2 and 18). The specific capacity for both the crystalline and nanocrystalline samples increases roughly linearly with x , however at very different rates. At the onset of nanocrystallinity, the capacity increases rapidly with x , which indicates a much higher Sn utilization. Presumably the Li is now reacting with the Sn atoms that are in the nanocrystalline regions. These electrochemical results correlate very well with the XRD results that also show the onset of the nanocrystalline region at the same point.

Galvanostatic Intermittent Titration Technique (GITT) Results

Figures 7d, e, and f, Fig. 11c, and Fig. 20d, e, and f show that the first discharge of $\text{Li}/\text{Mo}_{1-x}\text{Sn}_x$ cells with electrodes of nanocrystalline $\text{Mo}_{1-x}\text{Sn}_x$ ($x > 0.37$) is different than the subsequent cycles. In order to understand why this might be the case, we measured quasi-open-circuit voltage curves for $\text{Li}/\text{Mo}_{1-x}\text{Sn}_x$ cells with electrodes from film SPF66. Figure 26 shows that even with a 10 h relaxation period, the first discharge is still substantially different than the subsequent cycles. We believe that this is caused by the initial local expansion of the nanoscopic clusters of Sn as they react with Li, within the matrix of nanoscopic BCC phase that reacts with much less Li. This local expansion will lead to irreversible deformations of the host matrix and hence the latter cycles, once the deformations have already occurred, will be different from the first. It is worth noting that the first discharge and the latter cycles are quite similar for the crystalline BCC $\text{Mo}_{1-x}\text{Sn}_x$ samples, such as the sample with $x = 0.36$ shown in Fig. 11b. In this case, we believe a topotactic insertion mechanism is operative, so no significant differences between first and latter cycles are expected.

Conclusions

Sputter-deposition-based combinatorial techniques were used to prepare thin films of $\text{Mo}_{1-x}\text{Sn}_x\text{O}_y$ with different crystallinity and values of x and y . The reaction mechanism, specific capacity, and cycling behavior of the $\text{Mo}_{1-x}\text{Sn}_x$ thin films depend on the structure and oxygen content of the films.

In the case of crystalline BCC $\text{Mo}_{1-x}\text{Sn}_x$ ($x < 0.4$), the reaction with Li is believed to occur via a topotactic insertion mechanism into the BCC host structure. XRD studies, performed during discharge and charge, showed that host lattice expands and contracts as Li is inserted and removed. No other crystalline phases were observed to form. The capacity of the crystalline BCC phase is approximately 1 Li atom per Sn atom, quite smaller than the alloying limit of 4.2 Li per Sn.

The nanocrystalline materials, consisting of nanoscopic clusters of Sn and nanoscopic regions of the BCC phase, had a much higher Sn utilization; however Sn aggregation occurred and this leads to a loss of capacity during extended cycling.

Samples sputtered at high argon pressure were found to oxidize after the films were exposed to air. For $\text{Mo}_{1-x}\text{Sn}_x\text{O}_{0.4}$, a displacement reaction between Li and molybdenum oxide occurs. Hysteresis in the voltage-capacity behavior of Li/ $\text{Mo}_{1-x}\text{Sn}_x\text{O}_{0.4}$ cells, typical for displacement reactions of Li in metal oxides, is observed.

The most exciting results were obtained for samples sputtered at intermediate pressure, presumably in the presence of oxygen or moisture in the chamber (film SPD74). These samples contained about 20 atom % oxygen when x in $\text{Mo}_{1-x}\text{Sn}_x$ was around 0.4. $[\text{Mo}_x\text{Sn}_{1-x}]_{0.8}\text{O}_{0.2}$ samples with x near 0.4 gave reversible capacities near 350 mAh/g (all at low potential), showed good cycling behavior and no evidence for the aggregation of Sn into larger clusters over 20 cycles. It is our opinion that the aggregation of Sn is prevented by the incorporated oxygen.

Nanocrystalline $\text{Mo}_{1-x}\text{Sn}_x\text{O}_y$ with optimized values of x and y could be subjects of further research. It would be particularly interesting to determine the optimum values of x to obtain high capacity and the optimum value of y to prevent Sn aggregation so good cycling would result. Although specific capacities obtained may not be much higher than graphite, perhaps in the range of 400-500 mAh/g, the volumetric capacity is much higher than graphite because the $\text{Mo}_{1-x}\text{Sn}_x$ materials have densities between 7 and 10 g/cm³. Although thin film sputtering is probably not practical for the production of electrode materials, much can be learned with regard to those compositions and structures that might be more suitable choices for high capacity Li-ion anode materials. For example,

nanocrystalline $\text{M}_{1-x}\text{Sn}_x$, where M = Ni, Cr, Nb, W, Ta, etc. are candidates for anode materials as well; however more detailed studies on such systems are needed. The practice of combinatorial materials science, here at Dalhousie University, should allow the efficient screening of such materials.

Acknowledgments

The authors acknowledge the financial support of NSERC and 3M Canada for this work.

Dalhousie University assisted in meeting the publication costs of this article.

References

1. R. A. Huggins, in *Handbook of Battery Materials*, J. O. Besenhard, Editor, Part III.1, p. 359, Wiley-VCH, Weinheim (1999).
2. J. Yang, M. Winter, and J. O. Besenhard, *Solid State Ionics*, **90**, 281 (1996).
3. O. Mao, R. L. Turner, I. A. Courtney, B. D. Fredericksen, M. I. Buckett, L. J. Krause, and J. R. Dahn, *Electrochem. Solid-State Lett.*, **2**, 3 (1999).
4. K. D. Kepler, J. T. Vaughey, and M. M. Thackeray, *Electrochem. Solid-State Lett.*, **2**, 307 (1999).
5. J. T. Vaughey, J. O'Hara, and M. M. Thackeray, *Electrochem. Solid-State Lett.*, **3**, 13 (2000).
6. D. Larcher, Y. L. Beaulieu, D. D. MacNeil, and J. R. Dahn, *J. Electrochem. Soc.*, **147**, 1658 (2000).
7. L. Fransson, E. Nordstrom, K. Edstrom, L. Haggstrom, J. T. Vaughey, and M. M. Thackeray, *J. Electrochem. Soc.*, **149**, A736 (2002).
8. K. C. Hewitt, L. Y. Beaulieu, and J. R. Dahn, *J. Electrochem. Soc.*, **148**, A402 (2001).
9. J. R. Dahn, R. L. Turner, O. Mao, R. A. Dunlap, A. E. George, M. M. Buckett, D. J. McClure, and L. J. Krause, *Thin Solid Films*, **408**, 111 (2002).
10. R. L. Turner, B. Amick, L. J. Krause, L. Christensen, and J. R. Dahn, Abstract 257, The Electrochemical Society Meeting Abstracts, Vol. 2001-2, San Francisco, CA, Sept 2-7, 2001.
11. L. A. Thompson and J. A. Ellman, *Chem. Rev. (Washington, D.C.)*, **96**, 550 (1996).
12. J. J. Hanak, *J. Mater. Sci.*, **5**, 964 (1970).
13. E. J. Amis, X. D. Xiang, and J. C. Zhao, *MRS Bull.*, **27**, 295 (2002).
14. E. Reddington, A. Sapienza, B. Gurau, R. Viswanathan, S. Sarangapani, E. S. Smotkin, and T. E. Mallouk, *Science*, **280**, 1735 (1998).
15. J. R. Dahn, S. Trussler, T. D. Hatchard, A. Bonakdarpour, J. N. Meuller-Neuhaus, K. C. Hewitt, and M. Fleischauer, *Chem. Mater.*, **14**, 3519 (2002).
16. A. Bonakdarpour, K. C. Hewitt, T. D. Hatchard, M. D. Fleischauer, and J. R. Dahn, *Thin Solid Films*, **440**, 11 (2003).
17. P. Poizot, S. Laelle, S. Grugeon, L. Dupont, and J.-M. Tarascon, *J. Power Sources*, **97-98**, 235 (2001).
18. M. N. Obrovac, R. A. Dunlap, R. J. Sanderson, and J. R. Dahn, *J. Electrochem. Soc.*, **148**, A576 (2001).
19. I. A. Courtney, W. R. McKinnon, and J. R. Dahn, *J. Electrochem. Soc.*, **146**, 59 (1999).
20. T. Schober and H. Wenzl in *Hydrogen in Metals (II)*, G. Alefeld, and J. Volkl, Editors, p. 15, Springer-Verlag, Berlin (1978).
21. N. Schönberg, *Acta Chem. Scand. (1947-1973)*, **8**, 617 (1954).
22. F. Leroux and L. F. Nazar, *Solid State Ionics*, **133**, 37 (2000).